Role of Iron in the Marquesas Island Mass Effect

Hirohiti Raapoto, Elodie Martinez, Anne Petrenko, Andrea M. Doglioli, Thomas Gorgues, Raphaëlle Sauzède, Keitapu Maamaatuaiahutapu, Christophe Maes, Christophe Menkès, Jérôme Lefèvre

JGR Oceans

RESEARCH ARTICLE
10.1029/2019JC015275

Role of Iron in the Marquesas Island Mass Effect

Hirohiti Raapoto[1], Elodie Martinez[2], Anne Petrenko[3], Andrea Doglioli[3], Thomas Gorgues[2], Raphaëlle Sauzède[4], Keitapu Maamaatuaiahutapu[5], Christophe Maes[2], Christophe Menkes[6], and Jérôme Lefèvre[6]

[1]UPF, IRD, ILM, Ifremer, Écosystèmes Insulaires Océaniens, Tahiti, French Polynesia, [2]Université Brest, Ifremer, CNRS, IRD, Laboratoire d'Océanographie Physique et Spatiale, IUEM, Brest, France, [3]Aix-Marseille University, Université de Toulon, CNRS, IRD, OSU PYTHEAS, Mediterranean Institute of Oceanography MIO, UM 110, 13288, Marseille, France, [4]Sorbonne Université, CNRS, Institut de la Mer de Villefranche, Laboratoire d'Océanographie de Villefranche, Villefranche-sur-Mer, France, [5]Université de la Polynésie française, GePaSud Laboratory, Tahiti, French Polynesia, [6]IRD/Sorbonne Universités, Nouméa, New Caledonia

Key Points:
- Characterizing the biological enhancement observed in the Marquesas archipelago using a coupled physical biogeochemical ocean model
- Revealing the importance of iron in the Marquesas island mass effect

Correspondence to:
H. Raapoto,
hirohiti.raapoto@upf.pf

Citation:
Raapoto, H., Martinez, E., Petrenko, A., Doglioli, A., Gorgues, T., Sauzède, R., et al. (2019). Role of iron in the Marquesas Island mass effect. *Journal of Geophysical Research: Oceans*, *124*, 7781–7796. https://doi.org/10.1029/2019JC015275

Received 20 MAY 2019
Accepted 13 OCT 2019
Accepted article online 15 NOV 2019
Published online 16 NOV 2019

Abstract A remarkable chlorophyll-a concentration (Chl, a proxy of phytoplankton biomass) plume can be noticed on remotely sensed ocean color observations at the boundary separating the equatorial mesotrophic from the subtropical oligotrophic waters in the central South Pacific Ocean. This prominent biological feature is known as the island mass effect of the Marquesas archipelago. Waters surrounding these islands present high macronutrient concentrations but an iron depletion. In this study, the origin of Chl enhancement is investigated using a modeling approach. Four simulations based on identical physical and biogeochemical forcings but with different iron sources are conducted and analyzed. Only simulations considering an iron input from the island sediments present similar patterns (despite being too weak) of vertical and horizontal Chl distributions as compared to biogeochemical-Argo profiling float and satellite observations. In addition, simulations with no other iron input than the boundary forcings reveal the relative importance of remote processes in modulating the seasonal pattern of Chl around the archipelago t hrough horizontal advection of nutrient-rich waters from the equator toward the archipelago and vertical mixing uplifting deep nutrient-rich waters toward the upper lit layer.

1. Introduction

In the central South Pacific, the Marquesas archipelago (144–137°W/8–11°S) is located in the northern part of French Polynesia where the South Equatorial Current (SEC) flows south-westward. It is composed by a dozen of small volcanic islands with no surrounded coral reefs. The islands are characterized by rugged steep cliffs and high volcanic mountains up to 1,224 m (Maury et al., 2014). The main four islands are Nuku Hiva (339 km^2), Ua Pou (105 km^2), and Ua Huka (83 km^2) in the northern part of the archipelago and Hiva Oa (320 km^2) in the southern region (Figure 1a). One singular characteristic of the Marquesas archipelago is the remarkable plume of chlorophyll-a concentration (Chl, used as a proxy of phytoplankton biomass) that can be observed leeward of the islands on satellite ocean color observations (Figure 1b) (Signorini et al., 1999). Such localized increase of the biological activity around oceanic islands is commonly referred to an island mass effect (IME) (Doty & Oguri, 1956).

Located slightly north of the boundary between the equatorial mesotrophic waters and the oligotrophic subtropical gyre, the Marquesas Islands are lying in an HNLC (high-nutrient, low chlorophyll) environment (Claustre et al., 2008). In situ measurements are sparse in this remote area. However, relatively recent cruises have helped to improve our knowledge of the Marquesas archipelago environment. The oceanographic cruise BIOSOPE (Biogeochemistry and Optics South Pacific Experiment, devoted to study the biogeochemical properties in the South Pacific) crossed the Marquesas Islands and performed vertical profiles of nutrient at one station (see star in Figure 1a) westward of Nuku Hiva in 2004 (Claustre et al., 2008; Raimbault et al., 2007; Raimbault & Garcia, 2008), confirming the HNLC status of the waters surrounding the islands. Indeed, these profiles revealed high macronutrient concentrations in the surface layers with nitrate (NO3), phosphate (PO4), and silicate (Si) reaching, respectively, 2, 0.4, and 1 $\mu mol/L^1$. In 2012, a second oceanographic cruise *Pakaihi i te Moana* (PM-12) also measured elevated macronutrient concentrations in the archipelago and revealed a contrasted north/south gradient within the archipelago with higher concentrations of macronutrient and Chl in the north than in the south (Martinez et al., 2016).

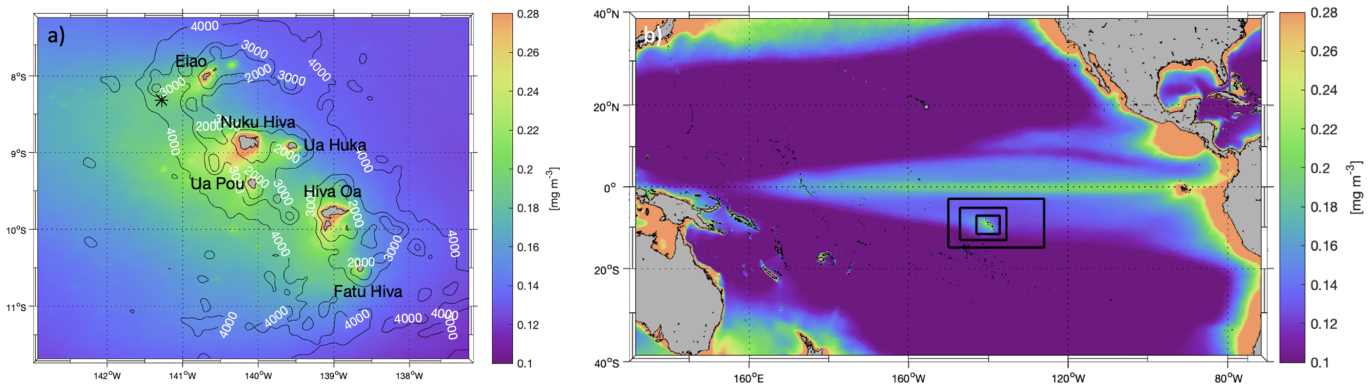

Figure 1. (a) Mean surface Chl from 1998 to 2015 over the Marquesas archipelago from GlobColour product (in mg/m^3). Black contours represent the bottom topography from the 2-arc minute topography/bathymetry data set ETOPO2 used in the model configuration. Depth values (in m) are indicated in white. The black star south-west of Eiao represents the MAR3 station from the BIOSOPE cruise. (b) Mean surface Chl as in (a) over the Pacific Ocean (in mg/m^3). The three embedded grids used in the model are represented by the three black boxes.

Contrary to macronutrient concentrations, weak dissolved iron concentrations (Fe) have been reported in the Marquesas ($0.15 < Fe < 0.41$ nmol/L) suggesting a possible limitation of phytoplankton growth by Fe (Blain et al., 2008). Indeed, similar IME have been investigated notably around islands in the Southern Ocean (i.e., Kerguelen, South Georgia, and Crozet Islands) where phytoplankton blooms regularly occur (Blain et al., 2007; D'Ovidio et al., 2015; Maraldi et al., 2009; Planquette et al., 2007; Robinson et al., 2016). In those cases, Fe fertilization by the islands has been incriminated to explain the observed intense blooms, whereas these islands are localized in HNLC areas. Indeed, it is now generally accepted that iron can act as a limiting micronutrient in HNLC regions (Boyd et al., 2000; Boyd et al., 2007; de Baar, 2005; Gordon et al., 1997).

When investigating the Marquesan IME through remote sensing observations, Martinez and Maamaatuaiahutapu (2004) associated the occurrence of Chl blooms with an intensification of the SEC. While these authors assumed that the mechanism at the origin of the blooms results from the interaction between the chain of islands and the mean flow, mechanisms were not clearly elucidated. Indeed, several physical processes can be involved in providing micro- and macronutrients to the euphotic zone, thus allowing the development of phytoplankton. Vertical mixing induced by eddies, jets, coastal upwelling, Ekman pumping, and internal wave breaking can play a key role in providing nutrient-rich water to the productive layer of the ocean (Barton, 2001; Benitez-Nelson & McGillicuddy, 2008; Hasegawa et al., 2009; Heywood et al., 1990, 1996; Palacios, 2002; Sangrà et al., 2001), but the precise role of these different mechanisms remains unclear in the archipelago.

The present work relies on the setup and analysis of the ocean dynamics through numerical modeling in the Marquesas region performed by Raapoto et al. (2018). Here, we aim at further developing our knowledge on the biogeochemistry component in this archipelago. Indeed, our study focuses on the role of different processes and more specifically the role of iron, in driving the development of the noticeable Chl plume characteristic of the Marquesan IME. Particular attention will be given to local versus remote mechanisms likely delivering iron to the upper lit layer of the ocean, thus allowing phytoplankton growth. This paper is organized as follows: Section 2 describes the physical-biological coupled numerical model, data, and methods. In section 3, the processes linking the seasonal variability of phytoplankton biomass to the macro- and micronutrients concentrations are presented and discussed. Finally, section 4 concludes this study.

2. Data and Methods

2.1. ROMS-PISCES

The physical model configuration used in this study is based on a three-dimensional primitive equations Regional Ocean Modeling System (ROMS, https://www.myroms.org) (Shchepetkin & McWilliams, 2005) configured for the Marquesas archipelago region. ROMS is a split-explicit, free surface, and terrain-following vertical coordinate oceanic model (Shchepetkin & McWilliams, 2003, 2005). We used the ROMS-AGRIF

(Adaptive Grid Refinement in Fortran) code provided by Debreu et al. (2012) and Penven et al. (2007). The AGRIF version is especially suitable to study the regional scale since it has the ability to manage an arbitrary number of fixed grids and embedding levels. We have used the two-way embedding procedure. It means that the parent grid provides the boundary conditions for the child grid and that the solution of the child grid is used to improve the larger scale parent grid solution. This allows a smooth and continuous interfacing between grid levels (Debreu et al., 2012; Debreu & Blayo, 2008). We defined three embedded grids for all simulations: (1) The first grid extends from 126 to 150°W and 3 to 15°S; (2) the second grid extends from 135.47 to 147.13°W and 5.24 to 13.19°S; and (3) the third grid extends from 137.16 to 142.98°W and 7.18 to 11.74°S (Figure 1b). The grid refinement rate is 3, implying a 1/5° (~22 km), 1/15° (~7 km), and 1/45° (~2.5 km) grid resolutions for the first, second, and third grid, respectively. This allows a sufficient sampling of the island topography and of the fine-scale dynamics, as the first baroclinic Rossby radius of deformation is about 120 km in this region according to Chelton et al. (1998). The 3 grids have 32 vertical levels and the vertical s-coordinate is stretched for boundary layer resolution. The topography is derived from the 2′ resolution ETOPO2 database provided by National Oceanic Atmospheric Administration-National Geographical Data Center (Smith & Sandwell, 1997). The bathymetry field has been filtered to keep the slope parameter <0.25 (Beckmann & Haidvogel, 1993). However, due to their size, the smallest islands such as Eiao and Fatu Hiva do not emerge and are only represented as seamounts in the model topography.

The physical model is then coupled to the "Pelagic Interaction Scheme for Carbon and Ecosystem Studies" (PISCES) biogeochemical model (Aumont et al., 2015). This biogeochemical model simulates the first trophic levels of the marine ecosystem and the biogeochemical cycles of carbon and the main nutrients. It has 24 compartments, of which 4 are living pools composed of 2 phytoplankton size-classes (nanophytoplankton and diatoms) and 2 zooplankton size-classes (microzooplankton and mesozooplankton). The phytoplankton growth is limited by five external nutrients concentrations (NO3, ammonium, PO4, Si, and Fe) and depends on light and temperature. The ratios between C, N, and P are kept constant to the values published in Takahashi et al. (1985). On the other hand, internal content of Chl, Fe, and Si (only for diatoms) in phytoplankton are prognostically simulated. The Chl/C ratio for the two phytoplankton groups is parameterized using the photo-adaptive model of Geider et al. (1997), while the Fe and Si phytoplankton contents are computed as a function of external concentrations and light levels. Nutrients are supplied to the ocean through three different processes: rivers, sediment mobilization, and dust deposition. Further details on the PISCES model functioning are available in Aumont et al. (2015). PISCES has been widely used in a variety of configurations from global scale simulations (e.g., Aumont & Bopp, 2006; Dufresne et al., 2013) to basin or regional scale studies, of which some were noticeably focused on the Pacific region (Dutheil et al., 2018; Gorgues et al., 2005; Gorgues et al., 2010).

The external physical forcings consist of monthly climatologies that have also been used and presented in Raapoto et al. (2018). At the surface, the heat and fresh water fluxes are extracted on a monthly ½° grid from the Comprehensive Ocean-Atmosphere Data Set (da Silva et al., 1994). The wind forcing is issued from the QuikSCAT monthly climatology calculated over 1999–2009, on a ¼° grid (Lungu & Callahan, 2006). The boundary conditions and initial state are based on the objective analysis of the World Ocean Atlas 2013 monthly climatology on a ¼° grid (Locarnini et al., 2013; Zweng et al., 2013). Initial and boundary conditions for the PISCES nutrients (phosphate, nitrate, and silicate) and oxygen are derived from the 2009 World Ocean Atlas monthly climatology (Garcia, Locarnini, Boyer, Antonov, Baranova, et al., 2010; Garcia, Locarnini, Boyer, Antonov, Zweng, et al., 2010). Dissolved iron is derived from global PISCES simulations that have been spun up to reach equilibrium (Aumont & Bopp, 2006). Aeolian dust deposition of iron to the ocean is estimated from the outputs of a dust deposition model (Tegen & Fung, 1995), which includes Africa, America, Asia, Australia, and Europe as dust sources (i.e., no dust from islands is considered). All those data have been preprocessed using the ROMSTOOLS toolbox (Penven et al., 2007) and are hereafter referred as WOA-PISCES.

2.2. Setup of the Four Biological Configurations

First, a comparison of the WOA-PISCES data set was performed with the only available in situ measurements of both micro- and macronutrients from the BIOSOPE oceanographic campaign at station MAR3 (Blain et al., 2008) (Figure 2). Samples at MAR3, located at 141.2777°W, 8.3213°S (Figure 1a), were collected on 29 October 2004.

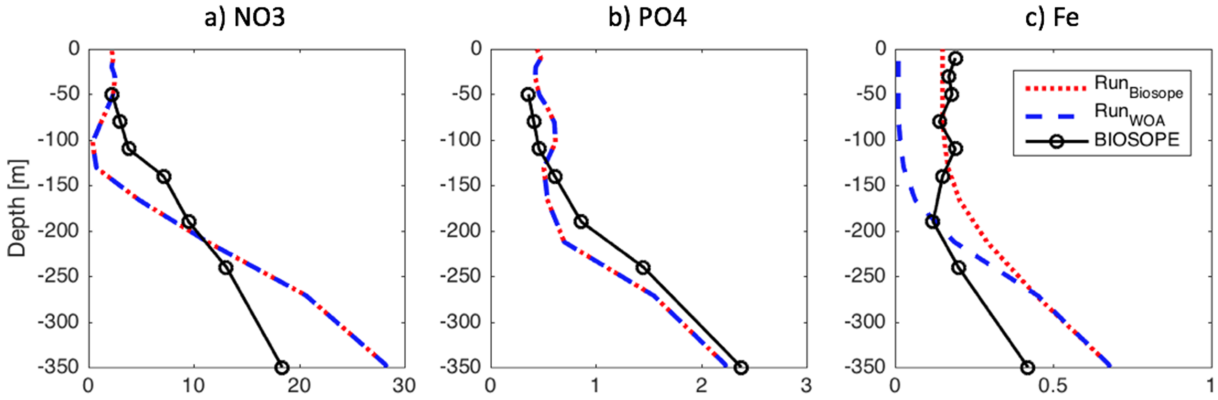

Figure 2. Vertical profiles of (a) NO3 (in μM), (b) PO4 (in μM), and (c) Fe (in nM) at MAR3 station on 29 October 2004 during BIOSOPE cruise (black curve – (S. Blain et al., 2008)) and from the forcing files of Run_{WOA} (blue dashed curve) and $Run_{Biosope}$ (red dotted curve) at the same location than MAR3 for the month of October. MAR3 is represented by a star on Figure 1a.

The MAR3 vertical profiles of NO3 and PO4 concentrations are close to the WOA-PISCES data in the upper 50 m (Figures 2a and 2b). NO3 profiles slightly differ around 100 m, while PO4 profiles remain close to the observations. NO3 and PO4 values are high enough to not limit phytoplankton growth as previously reported (Martinez et al., 2016; Raimbault et al., 2007; Raimbault & Garcia, 2008; Signorini et al., 1999). Fe concentrations are strongly underestimated from the surface down to 200 m in WOA-PISCES versus BIOSOPE data (Figure 2). Since it has been suggested that Fe is the limiting factor in the archipelago (Blain et al., 2008), the impact of Fe in the Marquesas IME is here investigated through four simulations with different Fe conditions:

- Run_{Ref}: is the reference simulation. It uses the WOA-PISCES Fe concentrations as initial and lateral boundary conditions. No sediment iron release whatsoever is considered.
- $Run_{Biosope}$: Fe is increased from the surface to the maximum gradient depth by adding 0.14 nmol/L^1 of Fe to fit with the BIOSOPE observations (Figure 2c). These values are imposed over the entire domain for the initial conditions and at the boundaries for the lateral forcing. No sediment iron release is considered.
- $Run_{Sed2.5}$: same as Run_{Ref} but a maximum Fe flux of 2.5 μmol·m^{-2}·day^{-1} is released from the sediment. This maximum value has been chosen in agreement with those obtained by Moore and Braucher (2008) and Aumont et al. (2015) by optimizing their biogeochemical modeling results with global Fe data sets (2 μmol·m^{-2}·day^{-1}).
- Run_{Sed5}: same as $Run_{Sed2.5}$ but applying a doubled Fe sediment flux of 5 μmol·m^{-2}·day^{-1}. Given the lack of data to constrain the sediment flux, this simulation was intended to document the sensitivity of our results to a higher iron flux.

In the latter two simulations, the PISCES sediment iron source from the bathymetry is constant over time. However, it has been made vertically variable in order to mimic the effect of oxygen levels in the sediments. Indeed, anoxic sediments (i.e., those one would find in the presence of high organic matter fluxes) are likely to release more iron to seawater (Elrod et al., 2004). The depth of each grid cell is then used as a proxy of the sediment oxygenation (Middelburg et al., 1996) resulting in an overall decrease toward greater depth of the iron flux from its maximum value.

Table 1 summarizes all the simulations performed. All simulations are run over 5 years with outputs averaged every 2 days. The iron concentration is stabilized after 1 year for the four simulations. Therefore, although $Run_{Biosope}$ has different initial conditions than the others, after 1 year, the initial field is not expected to play anymore a role in the interpretation of the results. The first 3 years, considered as the model spin-up, were removed from the following analysis.

2.3. Biogeochemical-Argo and Satellite Observations

Model outputs are compared with observations issued from a Biogeochemical-Argo (BGC-Argo) profiling float (Johnson & Claustre, 2016) that was deployed in August 2011 westward of Nuku Hiva and that drifted over 1.5 year within the archipelago (http://oao.obs-vlfr.fr/provbio/PAC_MQ_B25_9999999/PAC_MQ_

Table 1
Summary of the ROMS-PISCES Initial and Boundary Conditions Used in the Four Simulations

	Run_{Ref}	$Run_{Biosope}$	$Run_{Sed2.5}$	Run_{Sed5}
Physical initial and boundary conditions	WOA 2013			
Physical surface forcing	QSCAT			
Heat and fresh water flux	COADS			
Biological initial and boundary conditions (except the Fe compartment)	WOA-PISCES			
Fe compartment	WOA-PISCES	Fe initialization and boundary conditions modified from WOA-PISCES to fit the BIOSOPE observations in the upper layer	WOA-PISCES + a constant 2.5 $\mu mol \cdot m^{-2} \cdot day^{-1}$ Fe flux from sediment	WOA-PISCES + a constant 5 $\mu mol \cdot m^{-2} \cdot day^{-1}$ Fe flux from sediment

B25_9999999.html). The profiler has recorded daily data from 2 August 2011 to 09-23-2011 and every 5 days until 22 September 2012. This float was equipped with a seabird standard conductivity, temperature, and depth, completed with additional optical sensor packages including the WET Labs ECO Puck Triplet that noticeably measures the fluorescence of chlorophyll-*a*. The fluorescence observations were converted in Chl following the procedure described in Sauzède et al. (2018).

We also use satellite-derived Chl from GlobColour (http://www.globcolour.info). The weighted average of single-sensor level-2 Chl products merged from the Sea-Viewing Wide Field-of-View Sensor, Moderate Resolution Imaging Spectroradiometer, Medium Resolution Imaging Spectrometer, and *Visible Infrared Imaging Radiometer Suite* instruments from 1998 to 2015 increases the data coverage in both time and space. We use the 8-day composites with a spatial resolution of 4 km. Further details on the GlobColour data set can be found at the GlobColour website (http://www.globcolour.info/CDR_Docs/GlobCOLOUR_PUG.pdf). The satellite-derived Chl signal is strongly modulated by intra- and interannual variability in the Marquesas archipelago (Martinez et al., 2016). Therefore, the Chl seasonal signal has been extracted by performing a Fourier transform. All frequencies larger than a year have been removed, and the seasonal cycle has been reconstructed and is hereafter referred to $Chl_{GlobColour}$.

2.4. Dynamical and Biogeochemical Metrics

In this study, we define the eddy kinetic energy as the kinetic energy due to transient dynamic given by: $EKE = \frac{1}{2}\left(u'^2 + v'^2\right)$, where $u' = u - \overline{u}$ and $v' = v - \overline{v}$, u and v are the zonal and meridional components of the velocity at 10 m and $\overline{u}$ and $\overline{v}$ their annual mean from year 4 to 5.

The mixed layer depth (MLD) derived from model output is estimated according to the difference in potential density between 10 m and the base of the mixed layer using a threshold of 0.3 kg/m^3.

Remote sensing only allows the measurement of surface Chl in a layer defined from the surface to the first optical depth (Gordon & McCluney, 1975). This layer represents approximately the fifth of the euphotic layer (Morel & Berthon, 1989). To consistently compare satellite-derived $Chl_{GlobColour}$ and Chl from our simulations, a mean penetration depth has been derived from the euphotic depth. The euphotic depth was calculated using the exponential decrease of light along depth by determining the attenuation coefficient at 490 nm using the satellite Chl (Morel & Maritorena, 2001) and the associated total attenuation coefficient (Rochford et al., 2001; see details in Sauzède et al., 2016). Following this procedure, for surface Chl of 0.1 and 0.2 mg/m^3 (as observed on Figure 4b), the penetration depth reaches 17 and 13 m, respectively. Therefore, $Chl_{GlobColour}$ is compared with modeled Chl averaged over the first 15 meters of the water column.

3. Results and Discussion

3.1. Surface Ocean Dynamics

The four numerical simulations are initiated and forced with the same physical forcings than in Raapoto et al. (2018). Consequently, the ocean dynamics in these four simulations are similar and only briefly

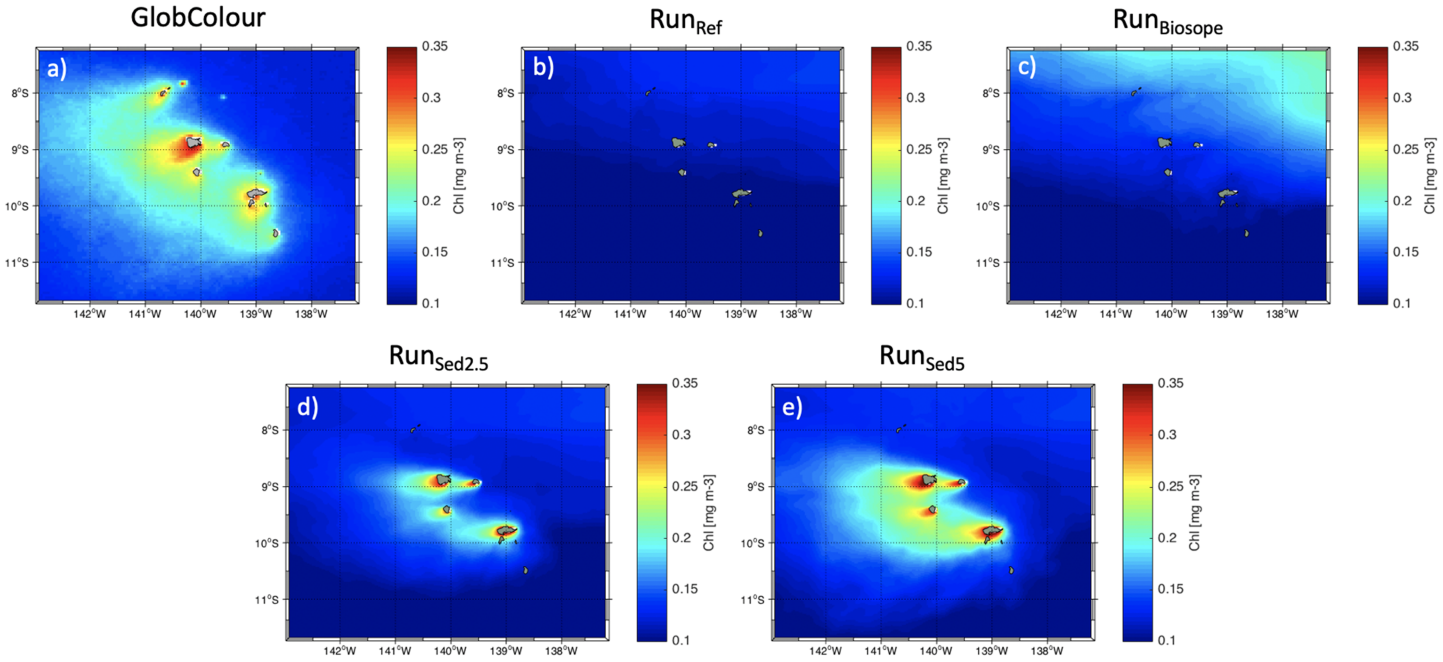

Figure 3. Annual mean over years 4 and 5 and at 10 m deep of (a) current (in m/s), (b) temperature (in °C), (c) EKE (in cm^2/s^2), and (d) vertical velocity (in m/day).

reminded here. For further details on the ocean dynamics, the reader is invited to refer to Raapoto et al. (2018).

The SEC flows southwestward with a stronger intensity in the northern part of the archipelago than in the south (~15 vs. 6 cm/s, respectively; Figure 3a). In the north, the SEC accelerates on the flanks of the islands and a region of weak current is observed just downstream the islands. Sea surface temperature exhibits in average colder water in the north (≤27.5°C) as the southward imprint of the equatorial upwelling (Wyrtki, 1981) and warmer water in the south (≥28°C) as the southeastward signature of the western Pacific warm pool (Yan et al., 1992) (Figure 3b). High mean eddy kinetic energy up to 95 cm^2/s^2 can be observed in the wake of the southern islands and at the northern boundary, south of the equator, with values up to 50 cm^2/s^2 (Figure 3c). The eddy activity is weaker elsewhere and noticeably in the wake of the northern islands. Mean vertical velocities are strong near the islands (Figure 3d), suggesting a strong impact of the bathymetry.

3.2. An Iron-Induced IME

Annual mean of satellite-derived $Chl_{GlobColour}$ is higher near the islands compared to the background concentrations (i.e., >0.3 vs. 0.1 mg/m^3, respectively), with a Chl plume extending south-westward, downstream the SEC (Figure 4a). This IME signature on Chl is not reproduced by the Run_{Ref} or $Run_{Biosope}$ model experiments, which present low Chl values all over the archipelago (Figures 4b and 4c). However, phytoplankton-enriched waters can be observed north-east of the archipelago in $Run_{Biosope}$. This is the result of the increased iron concentration (compared to Run_{Ref}) used to force this simulation. This higher amount of iron released at the north-eastern boundary is then advected southwestward by the SEC.

Adding Fe from the sediments in $Run_{Sed2.5}$ and Run_{Sed5} allows generating higher Chl in the vicinity of the islands as well as a Chl plume (characteristics of the IME) downstream the four main islands (Figures 4d and 4e). The extension of the simulated plumes is smaller than the observed one ($Chl_{GlobColour}$). There is no plume downstream the two smallest islands of Eiao, in the north, and Fatu Hiva, in the south, consistently with the already mentioned lack of representation of those islands in the model bathymetry. Doubling Fe input from the sediments from $Run_{Sed2.5}$ to Run_{Sed5} allows the closest reproduction of the IME signature observed from remote sensing. As a result, Fe input from the sediments appears to be a necessary condition in the model to reproduce the surface spatial structure of the IME observed from satellite radiometric observations.

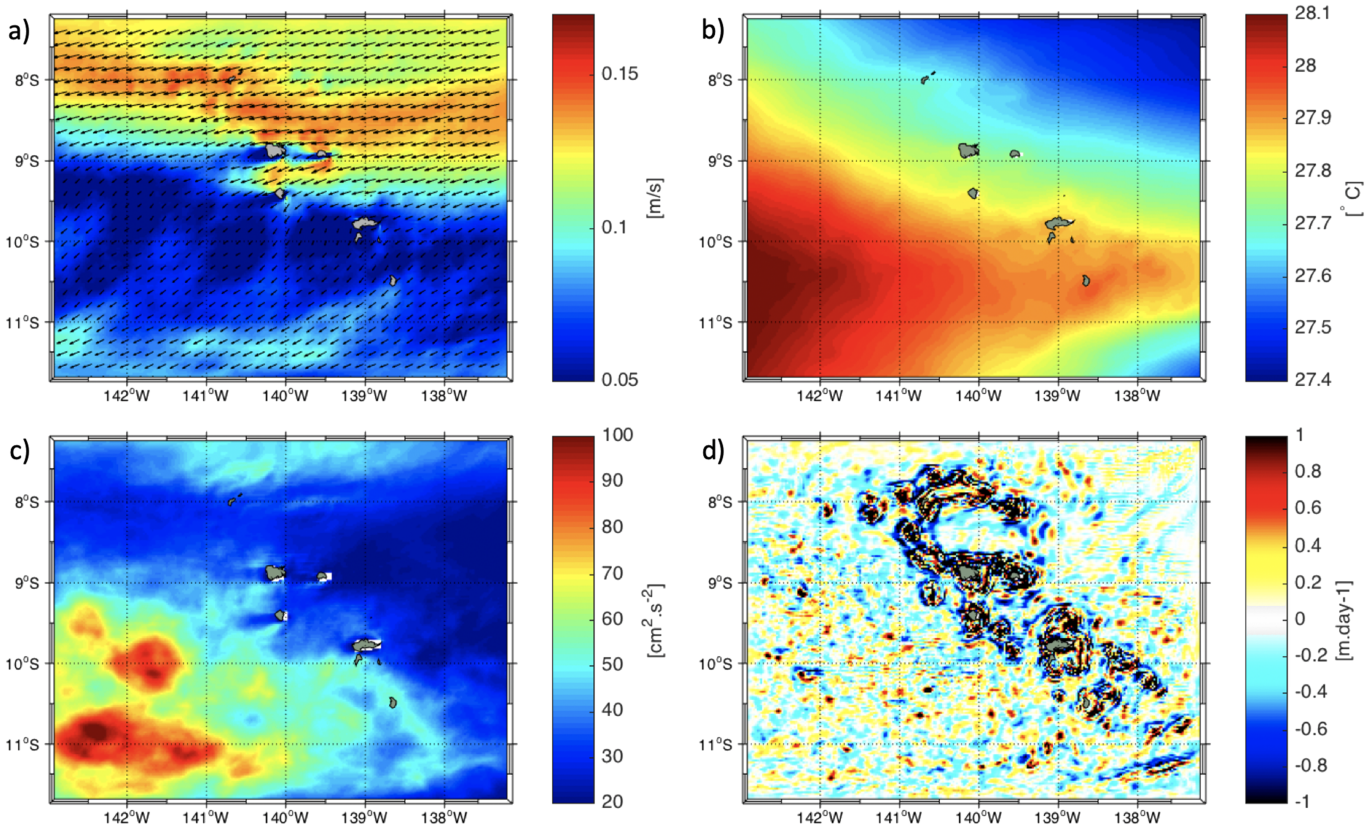

Figure 4. (a) Annual mean over 1998–2015 of surface $Chl_{GlobColour}$ in mg/m^3. Annual mean of Chl over year 4 to 5 for simulation (b) Run_{Ref}, (c) $Run_{Biosope}$, (d) $Run_{Sed2.5}$, and (e) Run_{Sed5}.

To provide an insight of the Chl vertical distribution within the archipelago, model outputs are compared with Chl observations issued from a BGC-Argo float (referred to $Chl_{BGC\text{-}Argo}$) released on 2 August 2011 leeward of Nuku Hiva (Figures 5a and 5b). The float trajectory is represented by crosses along time in Figure 5a. During approximately 2 months (late August to early October 2011), the float stayed in the lee of Nuku Hiva (Figures 5a and 5b) where surface currents are weak (Figure 3a). In this area, $Chl_{BGC\text{-}Argo}$ was higher than 0.5 mg/m^3 with peaks exceeding 1 mg/m^3 and with homogeneous profiles from the surface down to 70 m (Figure 5b). Similar patterns were observed as the float drifted southward away from Nuku Hiva, crossing the northern island wakes. In late February 2012, as the float drifted toward the southern islands of the archipelago, $Chl_{BGC\text{-}Argo}$ vertical profiles changed and started presenting a deep chlorophyll maximum (DCM) around 50–100 m, characteristic of more oligotrophic waters (Ras et al., 2008). $Chl_{BGC\text{-}Argo}$ vertical distribution alternated between well-mixed profiles and DCM profiles with weaker values than in the north. This north-south difference was also observed during the oceanographic cruise PM-12 where in situ Chl were stronger and homogeneous in the northern than in the southern part of the archipelago (Martinez et al., 2016).

Modeled Chl were sampled along the same trajectory than the BGC-Argo float and for the corresponding climatological dates. Chl maxima in the four simulations are at least twice lower than observations (Figures 5c–5f). Despite this common underestimation of Chl, the different simulations present contrasted vertical Chl patterns along the float trajectory. Chl from Run_{Ref} (hereafter Chl_{Ref}) presents a well-marked DCM over the whole trajectory with the highest values reaching 0.22 mg/m^3 (Figure 5c). Chl from $Run_{Biosope}$ (hereafter $Chl_{Biosope}$) exhibits similar patterns but with higher concentrations (~0.3 mg/m^3) due to higher Fe input at the boundaries (Figure 5d). Adding Fe from the sediments allows to (i) reproduce observed alternative periods of marked DCM and homogeneous profiles and (ii) highlight the north-south differences (Figures 5e–5f). Here again, Chl from Run_{Sed5} is closer to observations than from $Run_{Sed2.5}$

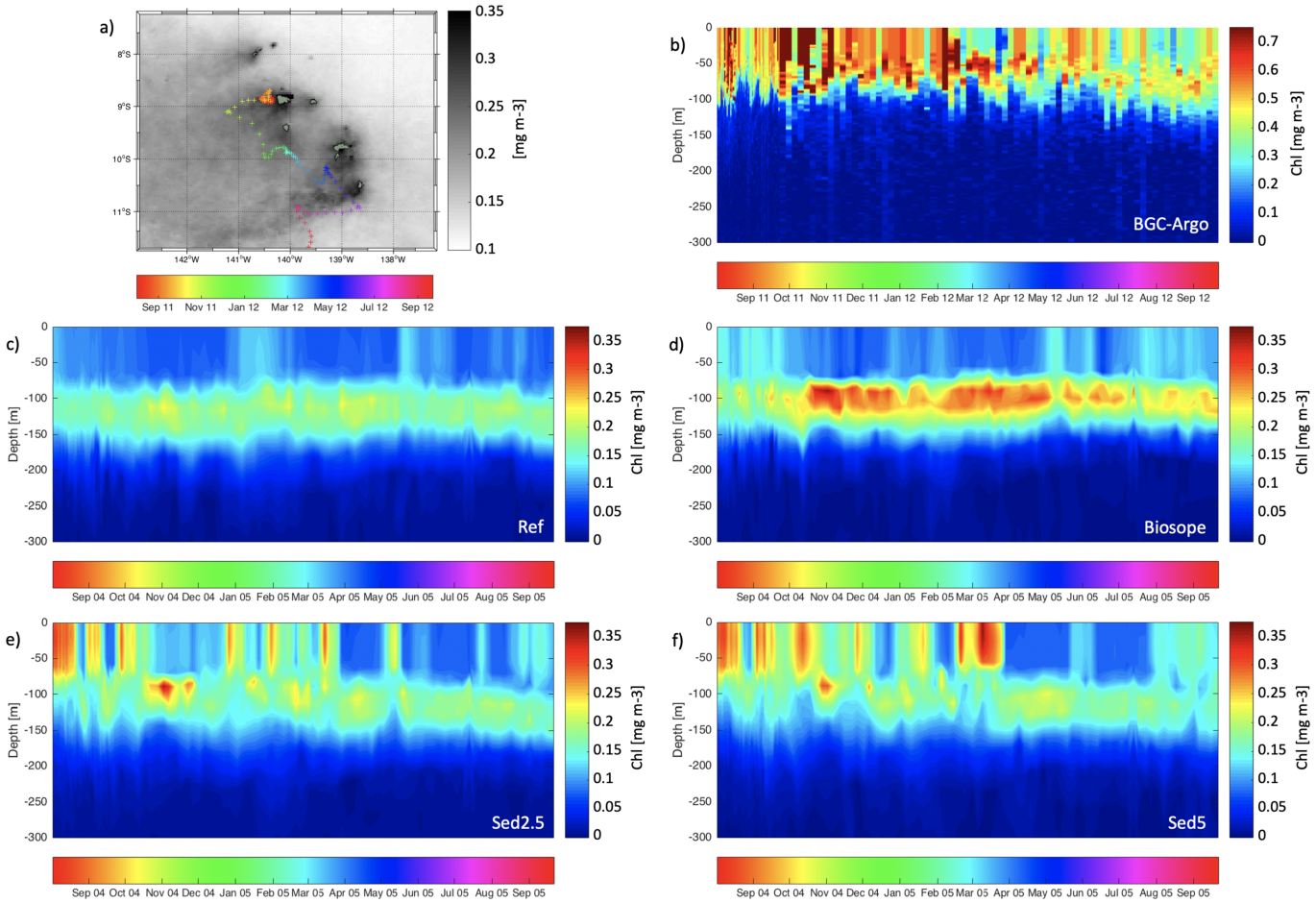

Figure 5. (a) Trajectory of the BGC-Argo float deployed west of Nuku Hiva on 2 August 2011 and drifting out south of the area on 22 September 2012. The corresponding dates are given by the horizontal color bar. Satellite-derived $Chl_{GlobColour}$ averaged over the BGC deployment time period is shown in background with the vertical gray scale. Vertical distribution along the BGC-Argo float trajectory of (b) $Chl_{BGC\text{-}Argo}$, (c) Chl_{Ref}, (d) $Chl_{Biosope}$, (e) $Chl_{Sed2.5}$, and (f) Chl_{Sed5} (in mg/m^3). The horizontal color bar in (b) gives the date of the above corresponding vertical profiles. The one used for simulations (c) to (f) refers to the climatological dates of the model. Note that, for clarity, the upper limit of the color bar used for the BGC-Argo float is twice larger than the one used for the simulations. BGC-Argo = Biogeochemical-Argo.

(hereafter Chl_{Sed5} and $Chl_{Sed2.5}$, respectively) due to the stronger Fe flux imposed from the sediments. The DCM is deeper in the four simulations than in the observations. Investigating the corresponding modeled NO3 and Fe fields (not shown), it appears that the depth of the nitracline is similar in the four simulations, while the depth of the ferricline is shallower by more than 80 m in $Run_{Biosope}$ than in the other three simulations. However, this shallower ferricline doesn't reflect on the $Run_{Biosope}$ DCM depth, suggesting it is light limited rather than iron limited. This result is consistent with a stronger surface Chl (which absorbs light), inducing a stronger light limitation and a shallower DCM in the observations than in the models. Still consistently in the models, an uplift of the DCM can be observed in Chl_{Sed5} when surface Chl significantly increases toward values closer to the observations.

In the model, a sediment iron source is then necessary to explain both the horizontal and vertical structure of the Marquesan IME. Nevertheless, Chl modeled from the four simulations still remains significantly weaker than observed $Chl_{BGC\text{-}Argo}$ and $Chl_{GlobColour}$.

3.3. Seasonal Variability of Phytoplankton

Here we intend to describe and decipher the physical and biogeochemical processes at regional and local scales explaining the Marquesas seasonal Chl variability.

3.3.1. Seasonal Variability Driven by Regional Physical Mechanisms

To further explore the physical mechanisms involved in the Chl seasonal variability in the Marquesas archipelago, physical and biogeochemical properties are investigated along a transect following the main flow direction and the temperature gradient and crossing the largest island, Nuku Hiva (NH-transect on Figure 6a).

Run_{Ref} shows an overall low annual mean of surface Fe (hereafter Fe_{Ref}, varying from 3 10^{-3} to 10 10^{-3} nmol/L; Figure 6a). A gradient with the highest values in the north-east is explained by relatively iron-rich water masses from the equatorial upwelling advected southwestward by the SEC. Chl_{Ref} patterns along the NH-transect are close upstream (north-east) and downstream (south-west) Nuku Hiva highlighting the absence of any IME imprint (Figures 6a and 6b). Chl_{Ref} distribution upstream is maximum in April and June with secondary increases in October and December and a minimum in September (Figure 6b). The downstream patterns show a time lag of 1 to 2 weeks compared with the upstream one. Indeed, Chl_{Ref} increases earlier at the northern boundary and then propagates southward. Chl_{Ref} increases concomitant with those of Fe, NO3, and PO4 concentrations (Figures 6c–6e). Si varies differently from other nutrients, particularly in May when it drops down to 2 μmol/L (Figure 6f). At this time period, nanophytoplankton contribution, which usually largely dominates (90%) the total phytoplankton biomass, decreases down to 80% (not shown). This is due to a higher supply of iron, NO3, and PO4 which allows a stronger growth of diatom (sensitive to Si) and consequently draws down Si.

In a general way, several physical mechanisms are likely to impact the phytoplankton seasonal variability. Among them, the horizontal advection of nutrient-rich waters from the equatorial area toward the archipelago allowing phytoplankton growth has been suggested by Signorini et al. (1999). Here, the surface SEC along the NH-transect strengthens up to 20 cm/s in April–May and June–July when nutrients and Chl_{Ref} also increase (Figures 7a and 7c with R_{SEC}- Chl_{Ref} = 0.35 upstream the island). This concomitant increase in time of the SEC and Chl_{Ref} in the archipelago is consistent with previously reported satellite observations (Martinez & Maamaatuaiahutapu, 2004), although these authors didn't provided any spatial glimpse of this advection process. Another conventional seasonal forcing (although never investigated in literature in the Marquesas) could be associated with convection processes allowing the vertical uplift of nutrient-rich waters from below the nutricline toward the upper lit layer and the subsequent phytoplankton growth. Consistently, when the MLD is the deepest in late November (down to 80 m – Figures 7b and 7c with R_{MLD}-Chl_{Ref} = 0.08 upstream the island) nutrients and Chl_{Ref} both increase (Figures 6b–6f and Figure 7 c). During this period, the macro- and micronutrient increase is weaker than in April–May and June–July, and the induced phytoplankton growth is consistently also weaker. These patterns are noticeable all along the transect, with a decrease southwestward (Figures 6, 7a, and 7b) following the north-east/south-west weakening of the HNLC properties as well as the SEC intensity.

In summary, seasonal nutrient supply toward the upper lit layer and the subsequent phytoplankton growth could be driven by both the southward SEC advection of equatorial nutrient-rich waters (in April–May and June–July), and the vertical uplift of nutrient-rich deep waters thanks to the deepening of the mixed layer (in November–December).

The amount of Fe added at the lateral boundaries in $Run_{Biosope}$ ($Fe_{Biosope}$) directly impacts $Chl_{Biosope}$ with higher values than Chl_{Ref} and a seasonal maximum exceeding 0.2 mg/m^3 upstream and downstream the transect crossing Nuku Hiva (Figure 8a). This increase also induces a stronger contribution of diatoms compared to Run_{Ref} (30% during $Chl_{Biosope}$ maximum, not shown). The Chl seasonal pattern upstream the island, likely induced by the equatorial advection and convection, is similar than in Run_{Ref}. $Run_{Biosope}$ differs from Run_{Ref} when considering the weakening of the first bloom. Chl_{Ref} decreases early May, simultaneously with Fe_{Ref}, $NO3_{Ref}$, and $PO4_{Ref}$. In $Run_{Biosope}$, macronutrients are also consumed in May, while $Fe_{Biosope}$ and $Chl_{Biosope}$ remain higher than 2 10^{-3} nmol/L and 0.2 mg/m^3, respectively. $Chl_{Biosope}$ only starts decreasing in early June, after both the macro- and micronutrient depletion. After that, in mid-June, the surface layer replenishes itself in macronutrients but not in micronutrients, while $Chl_{Biosope}$ remains low, suggesting again the role of Fe limitation.

In this simulation, Fe at the boundaries has been raised to fit the BIOSOPE measurements. However, concentrations obtained in the model outputs are still ten times inferior to the observations (Figure 8b vs.

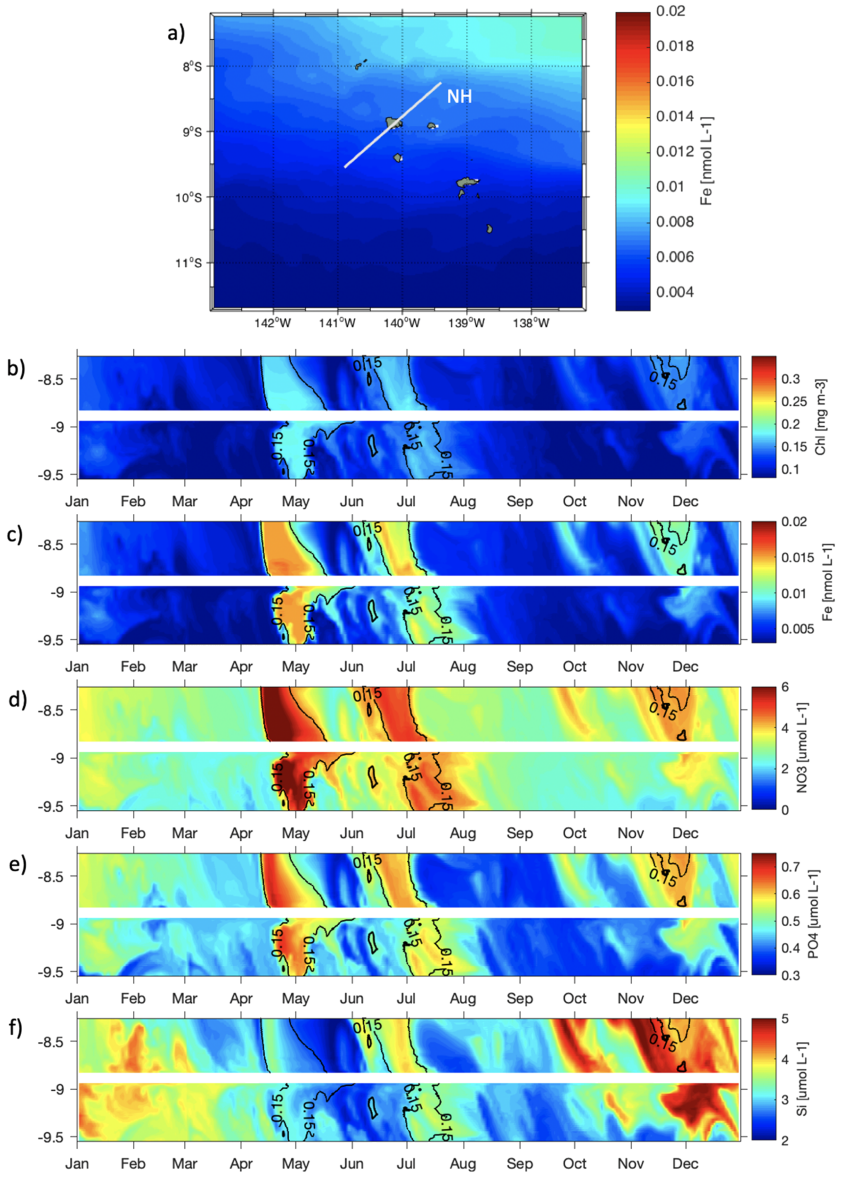

Figure 6. (a) Annual mean of Fe concentration in the archipelago during year 5 of Run_{Ref} at 10 m. The Nuku Hiva (NH)-transect is represented by the white line. Hovmöller diagrams along the NH-transect during year 5 of Run_{Ref} and at 10 m deep of (b) Chl (in mg/m^3), (c) Fe (in nM), (d) NO3 (in µmol/L), (e) PO4 (in µmol/L), and (f) Si (in µmol/L). The 0.15 mg/m^3 iso-contour of Chl_{Ref} is reported over all the Hovmöller diagrams.

Figure 2a). For the macronutrients, values along the NH-transect are weaker than in Run_{Ref}. Indeed, high $Fe_{Biosope}$ in these Fe depleted waters allows phytoplankton growth and a larger consumption of macronutrients. Here again, this configuration does not allow the generation of an IME but raises concerns on the Fe sources.

3.3.2. Seasonal Variability Modulated by Local Iron Sources

Because patterns presented in section 3.2 are the closest to observations in Run_{Sed5} when compared with $Run_{Sed2.5}$ (Figure 4 and Figure 5), hereafter we only focus on results from the Run_{Sed5} experiment.

Along the NH-transect, noticeable differences between the upstream and downstream Chl_{Sed5} averages are observed (Figure 9a). Upstream the island, Chl_{Sed5} time variability remains close to Chl_{Ref} and $Ch_{Biosope}$ (Figure 9a vs. 6b and 8a, respectively), supporting the idea of a minor role played by the local iron source (i.e., input from the sediments) in the seasonal variability simulated here. Indeed, the increase of Chl_{Sed5}

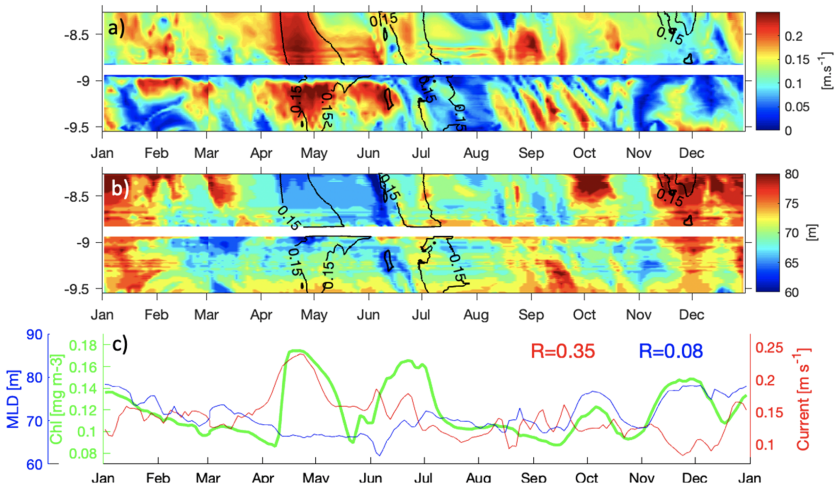

Figure 7. Hovmöller diagrams along the NH-transect during year 5 of Run_{Ref} of (a) current intensity (in m/s) at 10 m deep and (b) MLD (in m). The 0.15 mg/m iso-contour of Chl_{Ref} from Figure 6c is reported on (a) and (b). (c) Chl_{Ref}, MLD, and current intensity spatially averaged over the upstream NH-transect. Correlation coefficients of Chl_{Ref} versus the current intensity and versus the MLD are indicated in red and blue, respectively. MLD = mixed layer depth.

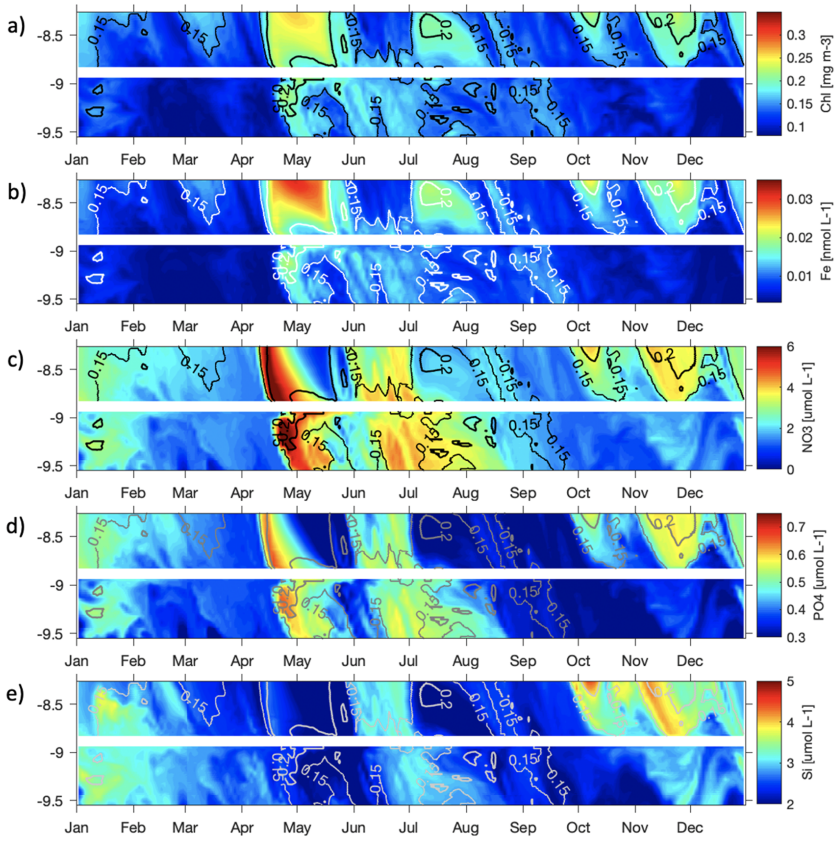

Figure 8. (a) Mean Chl concentration upstream and downstream of the island along NH-transect at −10 m for $Run_{Biosope}$. Latitude-time diagram of (b) Chl, (c) Fe, (d) NO3, (e) PO4, and (f) Si along NH-transect during year 5 of simulation at –10 m (units are in mg/m^3 for Chl and μmol/L for all the nutrients except Fe in nM). The 0.15 and 0.2 mg/m^3 iso-contours of $Chl_{Biosope}$ are drawn on the latitude-time diagrams.

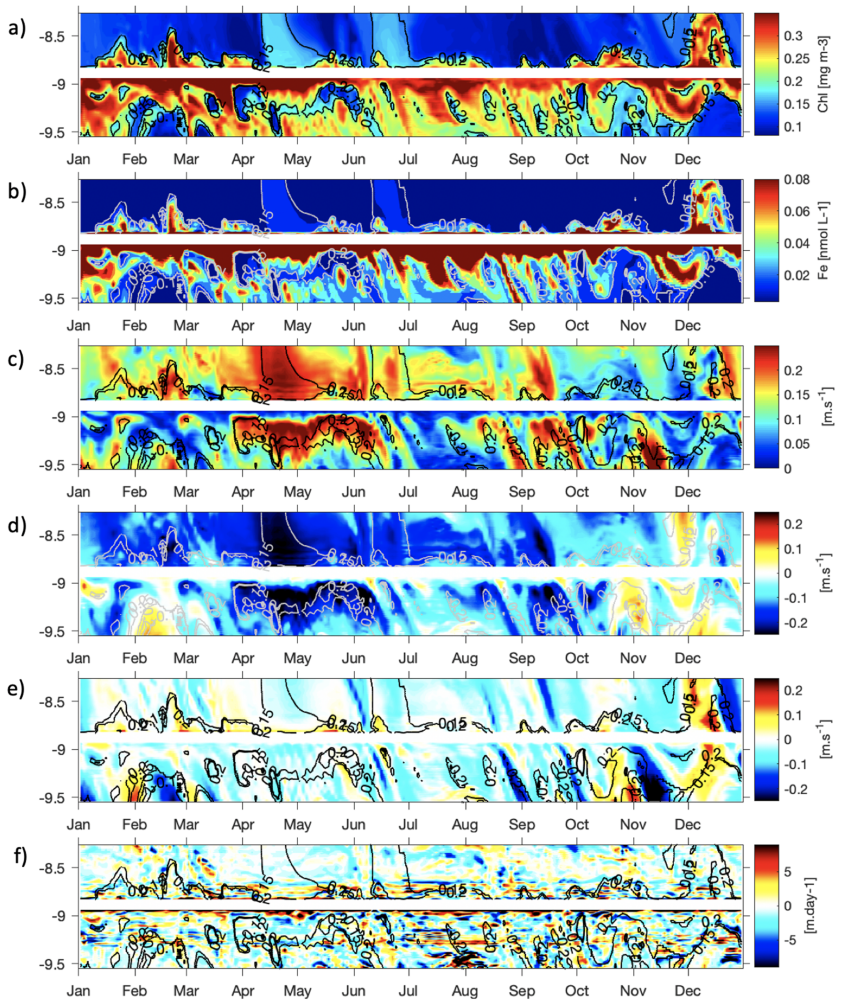

Figure 9. Hovmöller diagram of (a) Chl (mg/m^3), (b) Fe (nmol/L), (c) current intensity (m/s), (d) zonal current (m/s), (e) meridional current (m/s), and (f) vertical velocity (m/day) along the NH-transect as in Figures 6b–6f. The 0.15 and 0.2 mg/m^3 iso-contours of Chl_{Sed5} are reported on the Hovmöller diagrams.

and Fe_{Sed5} (Figure 9a and 9b) remains related with the SEC strengthening in late April and June and with the MLD deepening in late November. Unlike Run_{Ref}, Chl_{Sed5} and Fe_{Sed5} both increase in December. By that time, the meridional surface current becomes strongly positive inducing a northward flow (Figure 9e) and the transport of nutrients upstream the island. Upstream and close to the shore, high Chl_{Sed5} is the signature of the iron flux from the sediments.

Downstream Nuku Hiva, the input of Fe from the sediments allows a strong Chl_{Sed5} growth with values about twice higher than downstream (Figure 9a), again consistently with the IME imprint. The Chl seasonal variability observed upstream is here significantly impacted by iron injection and can't be distinguished anymore. In the very close shore, Chl_{Sed5} and Fe_{Sed5} remain high all over the year (Figures 9a and 9b) not only due to the constant flux of iron from the sediments but also due to a weak SEC (Figures 9c–9e) in the calm area just leeward the islands as identified in Figure 3a and by Raapoto et al. (2018). Downstream, further away from Nuku Hiva, a strengthening of the SEC along the transect may be related to contrasted effect on Fe_{Sed5} and Chl_{Sed5}, which, for instance, decrease in April to June while they increase in September (Figures 9a–9c). In fact, these two biogeochemical parameters show patterns likely propagating southward along the transect, and along time, concomitantly with a weaker than 0.1 m/s absolute zonal surface current (light blue and yellow in Figure 9d). This pattern tends to disappear when the zonal current intensifies (in dark blue and yellow-red). This suggests that high Fe_{Sed5} and Chl_{Sed5} initiated close to the island are

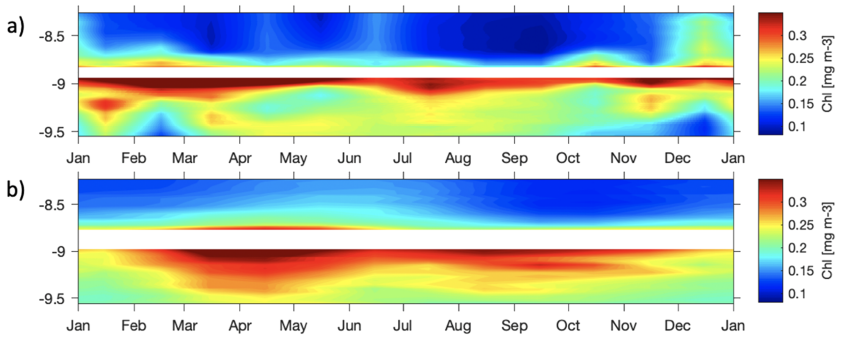

Figure 10. Latitude-time diagram of monthly average (a) Chl_{Sed5} over year 5 and (b) $Chl_{GlobColour}$ over 1998–2015 (mg/m^3).

zonally advected out of the transect, whether the intensification of the zonal current may be due to some regional strengthening of the SEC or to a more local mesoscale activity. Vertical velocities do not present specific patterns, except that they are generally positive very close to the island likely inducing an uplift of Fe toward the surface stronger along the southern coast (Figure 9f).

When comparing the seasonal variability of Chl_{Sed5} to satellite observations along the transect, patterns are reasonably close (Figure 10a vs. 10b). Upstream Nuku Hiva, $Chl_{GlobColour}$ and Chl_{Sed5} are both weaker in average than 0.2 mg/m^3. Some higher concentrations can be observed and, as illustrated in the previous paragraph, could be expected to be either related to a regional seasonal forcing or the northward advection of high Chl originating from the island. Downstream, both $Chl_{GlobColour}$ and Chl_{Sed5} are all year round significantly higher than 0.2 mg/m^3, highlighting the relatively well represented IME within $Run_{Sed5.}$ In the model, as well as in the observations, any existing regional seasonal signal illustrated upstream is downstream overwhelmed by the IME signature. However again, Chl_{Sed5} values are globally lower, and the southwestward extent of the plume is weaker than in the observations. In Run_{Sed5}, these high values remain near the island likely due to an insufficient Fe input or its chemical form (Gorgues et al., 2009; Jeandel & Oelkers, 2015).

4. Conclusion and Perspectives

In the present study, the origin and the seasonal variability of the IME occurring in the Marquesas archipelago are for the first time investigated setting up four climatological coupled ROMS-PISCES simulations. The four experiments use the same physical and biogeochemical forcings except for the Fe compartment. The first one is based on the WOA-PISCES data. The second one mimics a higher remote input of surface Fe in our domain through an increased iron concentration at the boundaries of our domain. Finally, a constant iron flux from the sediment is added in the third and fourth simulations. The biological enhancement induced by the islands and visible on remotely sensed observations is only represented in both simulations using an Fe input from the sediments. This is also the only way to reproduce the Chl vertical distributions alternating from homogenous profiles with high values in the upper layer of the northern archipelago to profiles associated with a DCM-like structure in the southern region as observed from a BGC-Argo profiling float. To the authors knowledge, the only existing iron data in the Marquesas region have been collected during the BIOSOPE cruise and published in Blain et al. (2008). In this latter study, the authors did not find any evidence of an iron sediment source from the Marquesas Islands sediments. However, at the scale of the archipelago, it is difficult to draw a synoptic view of the iron concentration from the only two stations sampled during the cruise. A close examination of the sampling location and time during the BIOSOPE cruise, in comparison with observed satellite Chl, shows that none of the stations were actually located in the chlorophyll plumes characteristic of the IME that we discuss in our study (not shown). A fair assumption would then be that specific circulation patterns at that time may have transported productive iron-enriched waters away from the sampling stations. The apparent discrepancy between our model outputs (focused on the Chl plume) and Blain et al.'s iron measurements may then only arise from sampling issue. Finally, at seasonal scale, modeled Chl regional variability appears to be likely driven by the southwestward advection of

rich waters from the equator and the deepening of the mixed layer uplifting nutrients toward the upper lit layer and allowing phytoplankton growth in the Marquesas. Nevertheless, this Chl seasonal pattern is scrambled downstream the island by the IME signature.

Several improvements may be considered regarding the Fe fluxes. First, several processes can be implied in the Fe input (e.g., river discharge, dust deposition, internal wave breaking, hydrothermal fluxes, etc.). However, there is no clear distinction made about the origin of the iron supply in the present simulations, since it is simply translated in the model by a supply from sediments. Thus, iron flux from the sediments was set constant along time and no seasonality of this iron source is considered here. However, process such as land drainage, which is a possible source of Fe supply, is expected to be stronger during the January to August rainy season (Laurent et al., 2004). Nevertheless, observations would be needed to truly evaluate these Fe fluxes and model them. Second, dissolved Fe is traditionally considered as the only available form for phytoplankton growth, while the role of the particulate Fe has been neglected. However, recent studies have highlighted the role of sediment inorganic particles dissolutions as a slow release of Fe at ocean margins (Gorgues et al., 2009; Jeandel & Oelkers, 2015). In the PISCES model (as in all biogeochemical models), this particulate inorganic fraction is not considered and could explain the spatial and amplitude underestimation of Chl_{Sed5} versus $Chl_{GlobColour}$. To partly resolve these issues of dissolved versus particulate iron, measurements were made as part of two oceanographic campaigns that took place in the Marquesas in Sep–Oct 2018 and Feb–March 2019 and may help to assess their impacts in the Marquesas IME.

Finally, because our study focused on the importance of a sediment iron source on the Marquesan IME, the present work didn't investigate the mesoscale and submesoscale processes at play in the plumes of high chlorophyll downstream the islands. Likewise, as we focused on the seasonal timescales, the impact of the interannual variability wasn't considered neither although the biological enrichment observed in the Marquesas archipelago can be influenced by El Niño Southern Oscillation (Legeckis et al., 2004; Martinez et al., 2018; Martinez & Maamaatuaiahutapu, 2004; Radenac et al., 2012; Signorini et al., 1999). To further investigate these two aspects, an interannual simulation of the coupled ROMS-PISCES model is currently ongoing. This last configuration would allow to investigate the impact of mesoscale processes on the biological enrichment in the Marquesas archipelago and their modulation by El Niño Southern Oscillation events.

Acknowledgments
We thank the government of French Polynesia for the financial support of the MOANA-MATY project (convention 6841/MTS) including the PhD grant of H. Raapoto. We also thank the OSU Pytheas that provided the cluster support. The data used in this work are available from the BGC-Argo profiling float (http://oao.obs-vlfr.fr/provbio/PAC_MQ_B25_9999999/PAC_MQ_B25_9999999.html) and satellite-derived chlorophyll-a from GlobColour (http://www.globcolour.info). The outputs of the numerical model used in this paper are available in eight parts on Zenodo.org (https://doi.org/10.5281/zenodo.3371766, https://doi.org/10.5281/zenodo.3384369, https://doi.org/10.5281/zenodo.3378062, https://doi.org/10.5281/zenodo.3385375, https://doi.org/10.5281/zenodo.3379190, https://doi.org/10.5281/zenodo.3386615, https://doi.org/10.5281/zenodo.3380531, and https://doi.org/10.5281/zenodo.3384373).

References

Aumont, O., & Bopp, L. (2006). Globalizing results from ocean in situ iron fertilization studies. *Global Biogeochemical Cycles*, *20*, GB2017. https://doi.org/10.1029/2005GB002591

Aumont, O., Ethé, C., & Tagliabue, a., Bopp, L., & Gehlen, M. (2015). PISCES-v2: An ocean biogeochemical model for carbon and ecosystem studies. *Geoscientific Model Development Discussions*, *8*(2), 1375–1509. https://doi.org/10.5194/gmdd-8-1375-2015

Barton, E. D. (2001). Island wakes. In J. Steele (Ed.), *Encyclopedia of ocean sciences* (Vol. 3, pp. 1397–1403). New York: Academic Press. https://doi.org/10.1006/rwos.2001.0140

Beckmann, A., & Haidvogel, D. B. (1993). Numerical simulation of flow around a tall isolated seamount. Part I: Problem formulation and model accuracy. *Journal of Physical Oceanography*, *23*(8), 1736–1753. https://doi.org/10.1175/1520-0485(1993)023<1736:NSOFAA>2.0.CO;2

Benitez-Nelson, C. R., & McGillicuddy, D. J. (2008). Mesoscale physical–biological–biogeochemical linkages in the open ocean: An introduction to the results of the E-flux and EDDIES programs. *Deep Sea Research Part II: Topical Studies in Oceanography*, *55*(10–13), 1133–1138. https://doi.org/10.1016/j.dsr2.2008.03.001

Blain, S., Bonnet, S., & Guieu, C. (2008). Dissolved iron distribution in the tropical and subtropical South Eastern Pacific. *Biogeosciences*, *5*(1), 269–280. https://doi.org/10.5194/bgd-4-2845-2007

Blain, S., Quéguiner, B., Armand, L., Belviso, S., Bombled, B., Bopp, L., et al. (2007). Effect of natural iron fertilization on carbon sequestration in the Southern Ocean. *Nature*, *446*(7139), 1070–1074. https://doi.org/10.1038/nature05700

Boyd, P. W., Jickells, T., Law, C. S., Blain, S., Boyle, E. A., Buesseler, K. O., et al. (2007). Mesoscale iron enrichment experiments 1993–2005: Synthesis and future directions. *Science*, *315*(5812), 612–617. https://doi.org/10.1126/science.1131669

Boyd, P. W., Watson, A. J., Law, C. S., Abraham, E. R., Trull, T., Murdoch, R., et al. (2000). A mesoscale phytoplankton bloom in the polar Southern Ocean stimulated by iron fertilization. *Nature*, *407*(6805), 695–702. https://doi.org/10.1038/35037500

Chelton, D. B., de Szoeke, R. A., Schlax, M. G., El Naggar, K., & Siwertz, N. (1998). Geographical variability of the first baroclinic Rossby radius of deformation. *Journal of Physical Oceanography*, *28*(3), 433–460. https://doi.org/10.1175/1520-0485(1998)028<0433:GVOTFB>2.0.CO;2

Claustre, H., Sciandra, A., & Vaulot, D. (2008). Introduction to the special section bio-optical and biogeochemical conditions in the South East Pacific in late 2004: The BIOSOPE program. *Biogeosciences*, *5*, 679–691. https://doi.org/10.5194/bgd-5-605-2008

da Silva, A. M., Young, C. C., & Levitus, S. (1994). Atlas of surface marine data 1994, vol. 4, Anomalies of fresh water fluxes. *Noaa Atlas Nesdis*, *9*, 308.

de Baar, H. J. W. (2005). Synthesis of iron fertilization experiments: From the iron age in the age of enlightenment. *Journal of Geophysical Research*, *110*, C09S16. https://doi.org/10.1029/2004JC002601

Debreu, L., & Blayo, E. (2008). Two-way embedding algorithms: A review. *Ocean Dynamics*, *58*(5–6), 415–428. https://doi.org/10.1007/s10236-008-0150-9

Debreu, L., Marchesiello, P., Penven, P., & Cambon, G. (2012). Two-way nesting in split-explicit ocean models: Algorithms, implementation and validation. *Ocean Modelling*, *49–50*, 1–21. https://doi.org/10.1016/j.ocemod.2012.03.003

Doty, M. S., & Oguri, M. (1956). The island mass effect. *ICES Journal of Marine Science*, *22*(1), 33–37. https://doi.org/10.1093/icesjms/22.1.33

D'Ovidio, F., Della Penna, A., Trull, T. W., Nencioli, F., Pujol, M. I., Rio, M. H., et al. (2015). The biogeochemical structuring role of horizontal stirring: Lagrangian perspectives on iron delivery downstream of the Kerguelen Plateau. *Biogeosciences*, *12*(19), 5567–5581. https://doi.org/10.5194/bg-12-5567-2015

Dufresne, J. L., Foujols, M. A., Denvil, S., Caubel, A., Marti, O., Aumont, O., et al. (2013). Climate change projections using the IPSL-CM5 earth system model: From CMIP3 to CMIP5. *Climate Dynamics*, *40*(9-10), 2123–2165. https://doi.org/10.1007/s00382-012-1636-1

Dutheil, C., Aumont, O., Gorguès, T., Lorrain, A., Bonnet, S., Rodier, M., et al. (2018). Modelling N2 fixation related to *Trichodesmium* sp.: Driving processes and impacts on primary production in the tropical Pacific Ocean. *Biogeosciences*, *15*(14), 4333–4352. https://doi.org/10.5194/bg-15-4333-2018

Elrod, V. A., Berelson, W. M., Coale, K. H., & Johnson, K. S. (2004). The flux of iron from continental shelf sediments: A missing source for global budgets. *Geophysical Research Letters*, *31*, L12307. https://doi.org/10.1029/2004GL020216

Garcia, H., Locarnini, R., Boyer, T., Antonov, T., Baranova, O., Zweng, M., & Johnson, D. (2010). WORLD OCEAN ATLAS 2009 Volume 3: Dissolved oxygen, apparent oxygen utilization, and oxygen saturation. World Ocean Atlas 2009.

Garcia, H. E., Locarnini, R. A., Boyer, T. P., Antonov, J. I., Zweng, M. M., Baranova, O. K., & Johnson, D. R. (2010). World Ocean Atlas 2009, Volume 4: Nutrients (phosphate, nitrate, silicate). *NOAA Atlas NESDIS*, *71*. https://doi.org/10.1182/blood-2011-06-357442

Geider, R. J., MacIntyre, H. L., & Kana, T. M. (1997). Dynamic model of phytoplankton growth and acclimation: Responses of the balanced growth rate and the chlorophyll a:carbon ratio to light, nutrient-limitation and temperature. *Marine Ecology Progress Series*, *148*(1–3), 187–200. https://doi.org/10.3354/meps148187

Gordon, H. R., & McCluney, W. R. (1975). estimation of the depth of sunlight penetration in the sea for remote sensing. *Applied Optics*, *14*(2), 413. https://doi.org/10.1364/AO.14.000413

Gordon, M., Coale, K., & Johnson, K. (1997). Iron in the equatorial Pacific: Implications for new production. *Limnology and Oceanography*, *42*, 419–431.

Gorgues, T, Menkes, C., Aumont, O., Slemons, L., & Murray, J. (2009). The iron phases, a crucial factor for the biomass variability in the Pacific HNLC region? In 2nd GEOTRACES Data—Model Synergy Workshop. https://doi.org/10.13140/2.1.5160.8322

Gorgues, T., Menkes, C., Aumont, O., Vialard, J., Dandonneau, Y., & Bopp, L. (2005). Biogeochemical impact of tropical instability waves in the equatorial Pacific. *Geophysical Research Letters*, *32*, L24615. https://doi.org/10.1029/2005GL024110

Gorgues, T., Menkes, C., Slemons, L., Aumont, O., Dandonneau, Y., Radenac, M. H., et al. (2010). Revisiting the La Ni??a 1998 phytoplankton blooms in the equatorial Pacific. *Deep-Sea Research Part I: Oceanographic Research Papers*, *57*(4), 567–576. https://doi.org/10.1016/j.dsr.2009.12.008

Hasegawa, D., Lewis, M. R., & Gangopadhyay, A. (2009). How islands cause phytoplankton to bloom in their wakes. *Geophysical Research Letters*, *36*, L20605. https://doi.org/10.1029/2009GL039743

Heywood, K. J., Barton, E. D., & Simpson, J. H. (1990). The effects of flow disturbance by an oceanic island. *Journal of Marine Research*, *48*, 55–73. https://doi.org/10.1357/002224090784984623

Heywood, K. J., Stevens, D. P., & Bigg, G. R. (1996). Eddy formation behind the tropical island of Aldabra. *Deep-Sea Research Part I: Oceanographic Research Papers*, *43*(4), 555–578. https://doi.org/10.1016/0967-0637(96)00097-0

Jeandel, C., & Oelkers, E. H. (2015). The influence of terrigenous particulate material dissolution on ocean chemistry and global element cycles. *Chemical Geology*, *395*, 50–66. https://doi.org/10.1016/j.chemgeo.2014.12.001

Johnson, K., & Claustre, H. (2016). Bringing biogeochemistry into the Argo Age. *Eos*. https://doi.org/10.1029/2016EO062427

Laurent, V., Maamaatuaiahutapu, K., Maiau, J., & Varney, P. (2004). Atlas Climatologique de la Polynésie Française (Météo Fran).

Legeckis, R., Brown, C. W., Bonjean, F., & Johnson, E. S. (2004). The influence of tropical instability waves on phytoplankton blooms in the wake of the Marquesas Islands during 1998 and on the currents observed during the drift of the Kon-Tiki in 1947. *Geophysical Research Letters*, *31*, L23307. https://doi.org/10.1029/2004GL021637

Locarnini, R. A., Mishonov, A. V., Antonov, J. I., Boyer, T. P., Garcia, H. E., Baranova, O. K., et al. (2013). World Ocean Atlas 2013. Vol. 1: Temperature. S. Levitus, Ed.; A. Mishonov, Technical Ed.; NOAA Atlas NESDIS, 73(September), 40. https://doi.org/10.1182/blood-2011-06-357442

Lungu, T., & Callahan, P. S. (2006). QuikSCAT science data product user's manual: Overview and geophysical data products. *D-18053-Rev A, Version*, *3*, 91.

Maraldi, C., Mongin, M., Coleman, R., & Testut, L. (2009). The influence of lateral mixing on a phytoplankton bloom: Distribution in the Kerguelen Plateau region. *Deep-Sea Research Part I: Oceanographic Research Papers*, *56*(6), 963–973. https://doi.org/10.1016/j.dsr.2008.12.018

Martinez, E., & Maamaatuaiahutapu, K. (2004). Island mass effect in the Marquesas Islands: Time variation. *Geophysical Research Letters*, *31*, L18307. https://doi.org/10.1029/2004GL020682

Martinez, E., Raapoto, H., Maes, C., & Maamaatuaihutapu, K. (2018). Influence of tropical instability waves on phytoplankton biomass near the Marquesas Islands, 1–12. https://doi.org/10.3390/rs10040640

Martinez, E., Rodier, M., & Maamaatuaiahutapu, K. (2016). Environnement océanique des Marquises. In R. Galzin, S.-D. Duron, & J.-Y. Meyer (Eds.), *Biodiversité terrestre et marine des îles Marquises, Polynésie Française* (pp. 123–136). Paris: Société française d'Ichtyologie.

Maury, R. C., Guille, G., Hervé, G., Catherine, C., Legendre, C., Rossi, P., et al. (2014). Géologie des Marquises : des volcans boucliers intra-océaniques effondrés issus d ' un point chaud atypique Géologie des Marquises: des volcans boucliers intra-océaniques effondrés issus d' un point chaud atypique. *Géologie de La France*, *1*(8), 111–135.

Middelburg, J. J., Soetaert, K., Herman, P. M. J., & Heip, C. H. R. (1996). Denitrification in marine sediments: A model study. *Global Biogeochemical Cycles*, *10*(4), 661–673. https://doi.org/10.1029/96GB02562

Moore, J. K., & Braucher, O. (2008). Sedimentary and mineral dust sources of dissolved iron to the world ocean to cite this version: Biogeosciences sedimentary and mineral dust sources of dissolved iron to the world ocean. *Biogeosciences*, *5*, 631–656.

Morel, A., & Berthon, J.-F. (1989). Surface pigments, algal biomass profiles, and potential production of the euphotic layer: Relationships reinvestigated in view of remote-sensing applications. *Limnology and Oceanography*, *34*(8), 1545–1562. https://doi.org/10.4319/lo.1989.34.8.1545

Morel, A., & Maritorena, S. (2001). Bio-optical properties of oceanic waters: A reappraisal. *Journal of Geophysical Research*, *106*(C4), 7163–7180. https://doi.org/10.1029/2000jc000319

Palacios, D. M. (2002). Factors influencing the island-mass effect of the Galápagos Archipelago. *Geophysical Research Letters*, *29*(23), 2134. https://doi.org/10.1029/2002GL016232

Penven, P., Marchesiello, P., Debreu, L., & Lefèvre, J. (2007). Software tools for pre- and post-processing of oceanic regional simulations. *Environmental Modelling and Software*, *23*(5), 660–662. https://doi.org/10.1016/j.envsoft.2007.07.004

Planquette, H., Statham, P. J., Fones, G. R., Charette, M. A., Moore, C. M., Salter, I., et al. (2007). Dissolved iron in the vicinity of the Crozet Islands, Southern Ocean. *Deep-Sea Research Part II: Topical Studies in Oceanography*, *54*(18–20), 1999–2019. https://doi.org/10.1016/j.dsr2.2007.06.019

Raapoto, H., Martinez, E., Petrenko, A., Doglioli, A. M., & Maes, C. (2018). Modeling the wake of the Marquesas archipelago. *Journal of Geophysical Research: Oceans*, *123*, 1213–1228. https://doi.org/10.1002/2017JC013285

Radenac, M. H., Léger, F., Singh, A., & Delcroix, T. (2012). Sea surface chlorophyll signature in the tropical Pacific during eastern and central Pacific ENSO events. *Journal of Geophysical Research*, *117*, C04007. https://doi.org/10.1029/2011JC007841

Raimbault, P., & Garcia, N. (2008). Evidence for efficient regenerated production and dinitrogen fixation in nitrogen-deficient waters of the South Pacific Ocean: Impact on new and export production estimates. *Biogeosciences*, *5*(2), 323–338. https://doi.org/10.5194/bg-5-323-2008

Raimbault, P., Garcia, N., & Cerutti, F. (2007). Distribution of inorganic and organic nutrients in the South Pacific Ocean—Evidence for long-term accumulation of organic matter in nitrogen-depleted waters. *Biogeosciences Discussions*, *4*(1), 3041–3087. https://doi.org/10.5194/bg-5-281-2008

Ras, J., Claustre, H., & Uitz, J. (2008). Spatial variability of phytoplankton pigment distributions in the subtropical South Pacific Ocean: Comparison between in situ and predicted data. *Biogeosciences*, *5*(2), 353–369. https://doi.org/10.5194/bg-5-353-2008

Robinson, J., Popova, E. E., Srokosz, M. A., & Yool, A. (2016). A tale of three islands: downstream natural iron fertilization in the Southern Ocean. *Journal of Geophysical Research: Oceans*, *121*, 3350–3371. https://doi.org/10.1002/2015JC011319

Rochford, P. A., Kara, A. B., Wallcraft, A. J., & Arnone, R. A. (2001). Importance of solar subsurface heating in ocean general circulation models. *Journal of Geophysical Research*, *106*(C12), 30923–30938. https://doi.org/10.1029/2000jc000355

Sangrà, P., Basterretxea, G., Pelegrí, J. L., & Arístegui, J. (2001). Chlorophyll increase due to internal waves on the shelf break of Gran Canaria (Canary Islands). *Signals*, *65*, 89–97. https://doi.org/http://digital.csic.es/bitstream/10261/5326/1/wave.pdf

Sauzède, R., Claustre, H., Uitz, J., Jamet, C., Dall'Olmo, G., D'Ortenzio, F., et al. (2016). A neural network-based method for merging ocean color and Argo data to extend surface bio-optical properties to depth: Retrieval of the particulate backscattering coefficient. *Journal of Geophysical Research: Oceans*, *121*, 2552–2571. https://doi.org/10.1002/2015JC011408

Sauzède, R., Martinez, E., de Pasqueron Fommervault, O., Poteau, A., Mignot, A., Maes, C., et al. (2018). Seasonal dynamics and disturbance of phytoplankton biomass in the wake of Tahiti as observed by biogeochemical-Argo floats. *Biogeosciences Discussions*, 1–35. https://doi.org/10.5194/bg-2017-541

Shchepetkin, A. F., & McWilliams, J. C. (2003). A method for computing horizontal pressure-gradient force in an oceanic model with nonaligned vertical coordinate. *Journal of Geophysical Research*, *108*(C3), 3090. https://doi.org/10.1029/2001JC001047

Shchepetkin, A. F., & McWilliams, J. C. (2005). The regional oceanic modeling system (ROMS): A split-explicit, free-surface, topography-following-coordinate oceanic model. *Ocean~Model*, *9*, 347–404. https://doi.org/10.1016/j.ocemod.2004.08.002

Signorini, S. R., McClain, C. R., & Dandonneau, Y. (1999). Mixing and phytoplankton bloom in the wake of the Marquesas Islands. *Geophysical Research Letters*, *26*(20), 3121–3124. https://doi.org/10.1029/1999GL010470

Smith, W. H., & Sandwell, D. (1997). Global sea floor topography from satellite altimetry and ship depth soundings. *Science*, *277*(5334), 1956–1962. https://doi.org/10.1126/science.277.5334.1956

Takahashi, T., Broecker, W. S., & Langer, S. (1985). Redfield ratio based on chemical data from isopycnal surfaces. *Journal of Geophysical Research*, *90*(C4), 6907–6924. https://doi.org/10.1029/JC090iC04p06907

Tegen, I., & Fung, I. (1995). Contribution to the atmospheric mineral aerosol load from land surface modification. *Journal of Geophysical Research*, *100*(D9), 18707. https://doi.org/10.1029/95JD02051

Wyrtki, K. (1981). An estimate of equatorial upwelling in the Pacific. *Journal of Physical Oceanography*, *11*, 1205–1214.

Yan, X., Ho, C., Zheng, Q., & Klemas, V. (1992). Temperature and size variabilities of the western Pacific warm pool. *Science*, *258*(5088), 1643–1645. https://doi.org/10.1126/science.258.5088.1643

Zweng, M. M., Reagan, J. R., Antonov, J. I., Mishonov, A. V., Boyer, T. P., Garcia, H. E., et al. (2013). World Ocean Atlas 2013, Volume 2: Salinity. *NOAA Atlas NESDIS*, *119*(1), 227–237. https://doi.org/10.1182/blood-2011-06-357442